



Contrasting Nighttime Heterogeneous and Daytime Photochemical Aging Drive the Optical Evolution of Black Carbon

Yin Zhang^{1,2}, Jinghao Zhai^{1,3}, Yaling Zeng^{1,2}, Shao Shi^{1,2}, Baohua Cai^{1,2}, Ke Yang^{1,2}, Yu Yan^{1,2}, Xin Yuan^{1,2}, Tianlong Hu^{1,2}, Chen Wang^{1,2}, Tzung-May Fu^{1,2}, Lei Zhu^{1,2}, Huizhong Shen^{1,2}, Jianhuai Ye^{1,2}, and Xin Yang^{1,2}

¹Shenzhen Key Laboratory of Precision Measurement and Early Warning Technology for Urban Environmental Health Risks, School of Environmental Science and Engineering, Southern University of Science and Technology, Shenzhen 518055, China

²Guangdong Provincial Field Observation and Research Station for Coastal Atmosphere and Climate of the Greater Bay Area, Southern University of Science and Technology, Shenzhen, Guangdong, 518055, China

³Department of Geophysical Sciences, University of Chicago, Chicago 60637, IL, United States

Correspondence: Jinghao Zhai (jinghao@uchicago.edu) and Xin Yang (yangx@sustech.edu.cn)

Abstract. Black carbon (BC) particles play a critical role in the climate system, yet their atmospheric aging processes and consequent optical impacts in real-world atmospheres remain insufficiently understood. In this study, we present integrated single-particle measurements using a single particle soot photometer (SP2) and a single-particle aerosol mass spectrometer (SPAMS) during a field campaign in urban Shenzhen, China. The mean refractory BC (rBC) mass concentration during the sampling period was $1.2 \mu\text{g m}^{-3}$, with core mass median diameters (MMD) of 155–170 nm. The diurnal variation in the coating-to-core mass ratio (MR) indicated that BC underwent continuous aging. Nighttime aging was primarily driven by heterogeneous nitrate uptake, whereas daytime photochemical aging was characterized by condensation of nitrate, sulfate, and oxidized organics. Despite their distinct mechanisms, both aging pathways significantly elevated the MR and produced similar net enhancements in the mass absorption cross section (MAC) at 532 nm with an overnight increase of $\sim 0.8 \text{ m}^2 \text{ g}^{-1}$ and a daytime increase of $\sim 1.0 \text{ m}^2 \text{ g}^{-1}$. These comparable net increments were primarily due to the offsetting effect of intensive fresh emissions during the day. Specifically, the MAC enhancement rates driven by nighttime heterogeneous reactions and daytime photochemical aging were determined to be 0.34 and $0.59 \text{ m}^2 \text{ g}^{-1} \text{ h}^{-1}$, respectively. This study provides direct observational evidence of diurnally contrasting BC aging pathways and quantitatively constrains the optical enhancement rates under real urban conditions.

1 Introduction

Black carbon (BC), formed during the incomplete combustion of fossil fuels and biomass, represents a major constituent of fine particulate matter in the atmosphere (Bond and Bergstrom, 2006). Its role in both climate systems (Bond et al., 2013) and public health (Baumgartner et al., 2014) is increasingly recognized, as BC contributes substantially to radiative forcing and adverse health outcomes. Owing to its strong light absorption across the solar spectrum, BC is regarded as a potent warming agent in the atmosphere (Jacobson, 2001).



Throughout its atmospheric lifetime, BC undergoes dynamic physical and chemical transformations (Wang et al., 2021). Numerous studies have investigated changes in BC properties (Zhang et al., 2018; Sun et al., 2020; Popovicheva et al., 2025), and the mechanisms driving its transformation during aging (Gong et al., 2016; Li et al., 2019). Freshly emitted BC typically exhibits a fractal, chain-like aggregate structure (Wang et al., 2021; Wu et al., 2018). As aging proceeds, the infilling of material within the BC pores can lead to structural collapse and the formation of more compact, near-spherical particles. Continued exposure to atmospheric constituents promote the accumulation of inorganic and organic coatings, ultimately yielding core-shell structures (Riemer et al., 2010; Zhang et al., 2008). This progressive structural and chemical evolution fundamentally dictates the dynamic changes in BC optical properties, leading to enhanced light absorption (Cappa et al., 2012; Bond and Bergstrom, 2006; Fuller et al., 1999; Peng et al., 2016).

However, quantifying the impact of atmospheric aging on BC optical properties in real-world conditions remains challenging. In the ambient, BC particles are subject to the simultaneous influences of emissions, chemical transformation, transport, and removal processes. While optical models and controlled chamber experiments often predict substantial absorption enhancement for heavily coated BC, field observations frequently report much weaker enhancements, even at high MR (Cappa et al., 2012, 2019). A compelling explanation for this discrepancy is the complex heterogeneity of BC mixing state in real-world environments (Fierce et al., 2016; Zhai et al., 2022a). Meteorological variations and emissions also constantly alter the population heterogeneity of BC particles at a given site. This dynamic interplay significantly complicates the bulk optical response, often causing the actual absorption enhancement to fall short of theoretical expectations derived from homogeneously mixed assumptions.

While field observations typically capture bulk BC mixture of ambient BC that is difficult to differentiate, advanced instrumentation enables detailed characterization of individual particle properties. A suite of instruments has been developed for this purpose (Petzold et al., 2013), among which the single particle soot photometer (SP2) is widely used for real-time measurements of BC mass and mixing state at the single-particle level (Stephens et al., 2003; Schwarz et al., 2006; Sedlacek III et al., 2012). Complementing the physical information provided by the SP2, the soot particle aerosol mass spectrometer (SP-AMS) is utilized to characterize the chemical composition of BC-containing particles. Joint deployments of SP2 and SP-AMS have yielded high-resolution insights into BC mixing states and chemistry (Liu et al., 2014; Cappa et al., 2012, 2019). The single particle aerosol mass spectrometer (SPAMS, distinct from SP-AMS), provides real-time chemical characterization of individual particles (Zhai et al., 2022a, b). Compared with SP-AMS, which primarily measures ensemble composition, SPAMS resolves particle-to-particle heterogeneity and identifies chemical tracers critical for source apportionment. Gong et al. (2016) demonstrated that SP2 and SPAMS, when used together, can effectively capture rapid changes in BC coatings during pollution events. Despite the strong complementarity of these instruments, joint field deployments remain rare, leaving an observational gap.

In this study, we analyzed observational data collected during a period minimally influenced by long-range transport and dominated by local traffic emissions in Shenzhen, China, a coastal megacity exhibits a distinctive combination of emission sources and meteorological conditions typical of subtropical urban environments. The region is characterized by strong atmospheric oxidative capacity, where abundant precursors from intensive vehicular traffic drive vigorous photochemical activity



(Xue et al., 2016). By integrating SP2 and SPAMS measurements, we resolved the diurnal aging behavior of freshly emitted BC particles and identified the associated chemical processes governing their evolution. When combined with concurrent optical measurements, these observations enabled quantification of the rates of optical change induced by both nighttime heterogeneous processing and daytime photochemical aging. This research provides direct observational evidence that tracks the diurnal aging pathways of BC under real urban atmospheric conditions, quantifying the subsequent rate of optical enhancement.

2 Methods

2.1 Field Measurements

Field measurements were carried out at the Southern University of Science and Technology (22°32' N, 114°03' E) in Shenzhen, China, from 21 November to 10 December 2021. Situated in the urban core, the sampling site provides a representative profile of aerosol characteristics typical of densely populated regions within the Pearl River Delta (PRD).

Ambient aerosols were drawn through a diffusion drying prior to instrument sampling to minimize the influence of ambient humidity. Refractory black carbon (rBC) was characterized at the single-particle level using a SP2 (Droplet Measurement Technologies, Boulder, CO, USA). To obtain complementary chemical composition information for individual particles, a SPAMS (Hexin Analytical Instrument Co., Ltd., Guangdong, China) was deployed alongside the SP2. In parallel, a photoacoustic extinctionmeter (PAX; Droplet Measurement Technologies, USA), operating at a wavelength of 532 nm, was used to quantify the bulk optical properties of the collected aerosols. To maintain data accuracy and minimize potential instrumental drift during continuous sampling, routine calibrations and performance checks were conducted throughout the campaign.

Simultaneous measurements of gaseous pollutants (O_3 , NO, NO_2 , NO_x , and CO) and particulate matter ($PM_{2.5}$) were conducted at the site, together with meteorological parameters including temperature, relative humidity, wind speed, and wind direction. The mixing layer height (MLH) was obtained from the ERA5 hourly reanalysis dataset provided by the European Centre for Medium-Range Weather Forecasts (ECMWF). ERA5 data were retrieved at a horizontal resolution of $0.25^\circ \times 0.25^\circ$. The time series of MLH for the sampling site was extracted using the nearest-neighbor interpolation method. To assess the influence of regional air mass transport, 72-hour backward trajectory analyses were performed using the HYSPLIT-4 model (Hybrid Single-Particle Lagrangian Integrated Trajectory), developed by the Air Resources Laboratory (ARL) of the U.S. National Oceanic and Atmospheric Administration (NOAA), with arrival heights set at 100 meters above ground level. A detailed depiction of the site location, trajectory clusters, and meteorological frequency distributions is illustrated in Fig. S1.

2.2 SP2 data analysis

In this study, the mass concentration and mixing state of BC were determined using a SP2. This instrument quantifies BC mass via the laser-induced incandescence (LII) technique. For clarity, the BC measured by the SP2 is hereafter referred to as refractory BC (rBC).



The operational principles of the SP2 have been described in detail elsewhere (Liu et al., 2010; Schwarz et al., 2006). Calibration of the incandescence signal was performed using Aquadag[®] black carbon particles (Aqueous Deflocculated Acheson Graphite, manufactured by Acheson Inc., USA), which exhibit a stronger incandescent response than ambient BC for the same mass. To correct for this difference, a correction factor of 0.75 was applied (Laborde et al., 2012). The mass-equivalent diameter of the rBC core (D_c) was calculated from the measured rBC mass, assuming a particle density of 1.8 g cm^{-3} (Bond et al., 2013). Scattering signal calibration was conducted using polystyrene latex spheres (Nanosphere Size Standards, Duke Scientific Corp., Palo Alto, CA, USA) with diameters ranging from 50 to 600 nm. The distorted scattering signals generated by individual rBC particles were reconstructed using the leading-edge-only (LEO) fitting technique (Gao et al., 2007). The total particle diameter (D_p) was then derived by applying the measured D_c and reconstructed scattering signal to a core-shell Mie model, assuming a complex refractive index of $m = 2.26 + 1.26i$ for the rBC core (Moteki et al., 2010) and $m = 1.50 + 0i$ for the coating material (Laborde et al., 2012). Assuming the coating density of 1.5 g cm^{-3} and the core density of 1.8 g cm^{-3} (Cappa et al., 2012), the coating-to-core mass ratio (MR) was estimated over a defined time window using Eq. (1):

$$MR = \frac{\rho_{\text{coating}} \sum_{i=1}^N (D_{p,i}^3 - D_{c,i}^3)}{\rho_{\text{core}} \sum_{i=1}^N D_{c,i}^3} \quad (1)$$

where $D_{p,i}$ and $D_{c,i}$ represent the total particle diameter and the core diameter of an individual rBC particle, respectively. Notably, the MR presented here is not derived from direct measurements, but rather estimated based on SP2-derived parameters. As such, the estimated MR serves solely as an indicative proxy for assessing the mixing state of the bulk rBC population, rather than being used to calculate bulk optical properties.

To characterize the mass size distribution of rBC cores, the rBC mass detected by the SP2 was first allocated into discrete size bins spanning a diameter range of 70 to 500 nm. After calculating the mass concentration within each bin, the resulting size distribution was fitted with a lognormal function:

$$\frac{dM}{d \log D_c} = A \exp \left(- \frac{(\log D_c - \log D_0)^2}{2 \log^2 \sigma_g} \right) \quad (2)$$

where A represents the peak mass concentration of the fitted distribution, D_0 denotes the mass median diameter (MMD), and σ_g is the geometric standard deviation (GSD) derived for each defined time window.

2.3 SPAMS data analysis

To investigate the chemical composition of BC-containing particles, a SPAMS was operated alongside the SP2 during the observation period. The operating principles of SPAMS have been described elsewhere (Li et al., 2011; Zhai et al., 2023). Over the entire sampling period, a total of 3,159,731 single-particle mass spectra were collected. Elemental carbon (EC) ion fragments were used as key markers of BC-containing particles (Spencer and Prather, 2006). Particles exhibiting EC ion signals with a relative peak area (RPA) greater than 0.1 were classified as BC-containing particles. Based on this threshold, 501,559 such particles were identified, accounting for approximately 15.9% of the total particles detected by SPAMS. To further categorize the BC-containing particles, an adaptive resonance theory-based clustering algorithm (ART-2a) was employed (Song



et al., 1999). This clustering analysis ultimately resulted in three distinct groups: EC, ECOC-NO_x, and ECOC-SO_x. The parameters used for ART-2a clustering were as follows: a learning rate of 0.8, a vigilance factor of 0.05, and 20 iterations. The average mass spectral patterns of each particle type are shown in Fig. S2.

120 SPAMS exhibits optimal mass spectral detection efficiency for particles with aerodynamic diameters of 400-600 nm, the BC particles measured within this range are generally in an aged state. Temporal analysis shows that the number concentration of the EC cluster exhibits the strongest correlation with rBC number concentrations ($R^2 = 0.75$, Fig. S3). Given that EC particles typically preserve the initial chemical signatures of primary BC emissions, positive matrix factorization (PMF) analysis was applied to the relative peak areas (RPAs) of characteristic ion fragments within the EC cluster. By resolving the relative
125 contributions of these characteristic chemical peaks, we aimed to trace the specific aging mechanisms of freshly emitted BC. Detailed procedures and parameter settings related to the PMF analysis are provided in the Supporting Information.

2.4 Particle optical property

A PAX (Droplet Measurement Technologies, USA) operating at a wavelength of 532 nm, was employed for in-situ measurements of aerosol optical properties. The scattering and absorption channels were calibrated using polystyrene latex (PSL)
130 spheres and fullerene soot, respectively. The absorption coefficients measured by the PAX showed strong agreement with both the rBC mass concentrations derived from the SP2 ($R^2 = 0.95$) and the absorption coefficients calculated using a core-shell Mie model ($R^2 = 0.94$) (Fig. S4), indicating the reliability of the optical measurements. To quantify the absorption property of rBC, the mass absorption cross section (MAC) was calculated by combining the light absorption coefficient measured by the PAX with the rBC mass concentration derived from SP2, as follows:

$$135 \quad MAC = \frac{b_{abs}}{[rBC]} \quad (3)$$

where b_{abs} is the aerosol absorption coefficient measured by PAX and $[rBC]$ is the rBC mass concentration from SP2. Since some brown carbon (BrC) also absorbs light at 532 nm, the calculated MAC includes absorption attributable to non-BC components as well as enhancement due to the lensing effect (Zhai et al., 2025; Cappa et al., 2019). The calculated MAC were adjusted to minimize the impact of BrC light absorption, with the detailed procedure described in the Supporting Information.
140 To minimize uncertainty with low signal levels, data points corresponding to rBC mass concentrations below $0.3 \mu\text{g m}^{-3}$ were excluded from the MAC calculation, reflecting the limitations in optical measurement accuracy at low concentrations (Liu et al., 2019). The relative coating thickness of individual rBC particles was inferred based on the time lag between the peaks of the incandescence and scattering signals recorded by the SP2 (Fig. S5a). Particles exhibiting a lag time greater than $2 \mu\text{s}$ were classified as thickly coated. Assuming that freshly emitted BC corresponds to a thinly coated population under ambient
145 conditions, the intercept of the MAC obtained by extrapolating to a zero fraction thickly coated particles was interpreted as the MAC of fresh BC (Lan et al., 2013), yielding a value of $7.13 \text{ m}^2 \text{ g}^{-1}$ (Fig. S5b).



3 Results and discussion

3.1 Overview of sampling period

Figure 1 illustrates temporal variations in measured meteorological parameters (temperature, humidity, and wind speed) together with concentrations of PM_{2.5}, O₃, NO_x, CO, and rBC from 21 November to 9 December 2021. Based on 72-hour backward trajectory analyses, air masses were classified into three distinct clusters (Fig. S1a). Cluster 1 (C1), originating from the eastern coastal regions, dominated from 21 November through 7–9 December. Cluster 3 (C3) represented long-range transport from the northwestern interior, influencing the site during 22–25 November and 1–3 December. Periods influenced by C3 were characterized by decreasing temperatures and relative humidity, typical signatures of wintertime cold waves, accompanied by stronger wind speeds and lower rBC concentrations (Figs. 1b and S1b). Despite the lower rBC levels, elevated MR during these intervals suggests an increased proportion of aged BC particles. In contrast, Cluster 2 (C2), which accounted for 41.23% of the total sampling time, exhibited minimal spatial movement, thereby limiting the influence of long-range transport. Within the C2-dominated conditions, a continuous 7-day interval was identified (green box in Fig. 1) during which O₃, NO_x, CO and rBC all displayed consistent diurnal patterns. This period was therefore selected as a representative case dominated by the local emissions for detailed analysis of BC aging processes.

During this episode, ambient temperatures ranged from 11°C to 26°C (mean: 18°C), and relative humidity varied between 26% and 80% (mean: 55%) (Fig. 1a). The mean PM_{2.5} concentration was 31.3 μg m⁻³, indicating moderate pollution levels (Fig. 1b). The average rBC concentration was 1.2 μg m⁻³, contributing approximately 3.8% to the PM_{2.5} mass. Furthermore, rBC showed strong correlations with NO_x (R² = 0.71, *p* < 0.001) and CO (R² = 0.51, *p* < 0.001), both recognized tracers of vehicular emissions in urban environments (Gong et al., 2016; Laborde et al., 2013; Liu et al., 2014). Besides, the sampling site is located in a densely trafficked urban area without major industrial sources nearby. The site characteristics and the observed pollutant correlations strongly suggest that local traffic emissions were the primary source of rBC during this period. Characterized by consistent diurnal variations in both meteorology and pollutants, minimal long-range transport, and traffic-dominated BC emissions, this episode served as an ideal 'natural chamber'. Such unique conditions provided an exceptional opportunity to directly investigate the atmospheric aging of BC from an observational perspective.

The diurnal variations of meteorological parameters and pollutant concentrations are shown in Figure 2. While intense morning emissions were expected, the rBC concentration (Fig. 2c) exhibited a distinct bimodal pattern, with peaks occurring only during the evening rush hours (18:00–20:00 LT) and around midnight (00:00 LT). The absence of a morning peak is likely attributed to rapid dispersion associated with the rising mixing layer height (MLH) and wind speed (Fig. 2a, d). The midnight rBC peak coincided with significant increases in NO and CO concentrations (Fig. 2b, h). Given the lack of nearby industrial sources, this synchronized surge across NO and rBC likely points to emissions from heavy-duty diesel vehicles.

The size distribution of rBC cores further supports an urban traffic-dominated source. The MMD ranged from 155 to 170 nm (Fig. 2f) with relatively narrow and stable GSDs (1.55–1.58, Fig. S5), typical of urban vehicular sources (Li et al., 2023; Yang et al., 2022). A notable observation is the continuous increase of MMD in the nighttime from 155 to 170 nm. Normalized



180 size distributions (Fig. S5b) indicate that that the slight diurnal fluctuations in MMD were driven by the intermittent inputs of smaller, freshly emitted BC particles, rather than by regional transport.

Given the minimal influence of external transport, changes in the MR provides evidence of in-situ BC aging. The MR exhibited a continuous increase from 08:00 to 14:00 (Fig. 2i), correlated with O_x ($R^2 = 0.51$, Fig. S7), indicating that photochemical processing dominated daytime BC aging (Zhang et al., 2025). In addition, MR also increased during nighttime, suggesting
185 nocturnal aging of BC. Similar behavior has been reported in previous studies under conditions conducive to heterogeneous reactions (Liu et al., 2022; Wei et al., 2023).

Distinct aging pathways during day and night are further corroborated by the diurnal distribution of rBC coating thickness (Fig. 3). During nighttime, BC particles exhibited gradual growth, with the coating thickness of the dominant population increasing by 10 nm. In contrast, daytime BC particles exhibited thinner coatings, primarily due to continuous input of fresh
190 BC from intense daytime traffic emissions. Under photochemical conditions, however, a secondary mode emerged at a coating thickness of 60 nm. This heavily coated mode is likely governed by two factors: the accelerated photochemical aging of a subset of existing BC particles; and the diurnal expansion of the planetary boundary layer (PBL), which dilutes the freshly emitted BC and thereby elevates the relative number fraction of the aged mode. Although the precise contribution of PBL dilution remains challenging, the emergence of this bimodal distribution highlights the pronounced heterogeneity of BC mixing state
195 during daytime, in contrast to the more uniform coating characteristics observed at night.

3.2 Diurnal Aging Mechanisms of BC

The diurnal variations in the mixing state demonstrate that BC undergoes distinct daytime and nighttime aging processes. To further elucidate the chemical mechanisms driving these dynamic transformations, we examined the diurnal evolution of the chemical composition of BC-containing particles. The diurnal variation of OC closely tracked that of the BC mass
200 concentration (Fig. 2c). In contrast, oxygenated organic carbon (OOC) and sulfate (SO_4^{2-}) exhibited drastic increases during the daytime, indicative of secondary formation. Nitrate (NO_3^-) displayed a bimodal pattern, with one peak occurring at night and a second peak emerging during the early stages of daytime photochemistry. Ammonium (NH_4^+) increased concurrently during the day, aligning with the rising trends of both sulfate and nitrate. In comparison to non-BC particles (Fig. 4b), which share similar diurnal trends for other secondary species, BC-containing particles exhibit significantly greater RPA variability
205 exclusively for SO_4^{2-} . This distinct enhancement highlights that the BC surface specifically promotes sulfate formation (Guo et al., 2025; Zhang et al., 2021).

To further resolve the aging processes of freshly emitted BC, PMF analysis was applied to particles within the EC cluster. This approach decomposes complex mass spectral data into distinct chemical factors and their temporal contributions (Zauscher et al., 2013). The resulting factor profiles and diurnal patterns are shown in Fig. 5. A substantial increase in the Nitrate factor
210 was observed during nighttime, which is likely attributable to elevated NO_2 emissions during the evening rush hours. These emissions rapidly depleted O_3 (Fig. 2g), driving the formation of NO_3 radicals and the subsequent production of N_2O_5 (Wang et al., 2009). Heterogeneous hydrolysis of N_2O_5 on BC particle surface then promoted the rapid accumulation of nitrate (Yuan et al., 2020). During the early stage of daytime photochemical aging, the contribution of the nitrate factor began increasing



earlier than that of the Sulfate–OOC factor. This temporal offset may be explained by two possible mechanisms: (1) SO_4^{2-} precursors may not have reached sufficient concentrations at that time (Zhang et al., 2021; Zhou et al., 2022); and (2) gaseous HNO_3 formed via photochemical reactions may have been directly taken up by BC particles through heterogeneous processes (Choi and Leu, 1998; Prince et al., 2002). However, the available observations do not permit a definitive determination of the dominant pathway. The Sulfate–OOC factor reached its maximum between 11:00 and 14:00 LT, coinciding with a pronounced increase in the ammonium factor. This concurrence suggests enhanced formation of $(\text{NH}_4)_2\text{SO}_4$ and other secondary photochemical products, leading to accelerated BC aging through condensational growth.

In alignment with the bulk BC-containing particle population, the primary EC cluster exhibits similar trends in secondary species accumulation. This consistency across different analytical approaches explicitly highlights the highly dynamic nature of BC aging, pointing to distinct chemical evolutionary pathways operating under daytime and nighttime atmospheric conditions.

3.3 Diurnal Variations of BC optical properties

The diurnal aging of BC observed during the sampling period was accompanied by corresponding changes in its optical properties. As shown in Fig. 6a, the MAC reached a minimum of $8.1 \text{ m}^2 \text{ g}^{-1}$ at 22:00 LT. Thereafter, it increased by $\sim 0.8 \text{ m}^2 \text{ g}^{-1}$ overnight, reaching $\sim 8.9 \text{ m}^2 \text{ g}^{-1}$ by 06:00 LT. A comparable enhancement occurred during the daytime photochemically active period, when MAC increased by $\sim 1.0 \text{ m}^2 \text{ g}^{-1}$, from 8.9 to $9.9 \text{ m}^2 \text{ g}^{-1}$. While photochemical aging generally proceeds more rapidly than nighttime heterogeneous processing, the comparable increases in MAC during both periods indicate that multiple atmospheric processes jointly influence the evolution of BC optical properties.

BC particles in the early stages of aging exhibit negligible light absorption enhancement (Peng et al., 2016; Liu et al., 2017; Wu et al., 2018). Based on the MR threshold of 3 proposed by Liu et al. (2017) for significant lensing-induced absorption enhancement, the mass fraction of rBC with $\text{MR} > 3$ increased from 0.32 to 0.35 during the night, decreased to 0.32 following the morning rush hour, and subsequently rose to 0.40 after daytime photochemical aging. Notably, the magnitude of this diurnal change is substantially larger than the observed day-night variation in bulk MAC.

In the ambient atmosphere, the bulk optical properties of BC are influenced not only by aging but also by emissions, regional transport, and removing processes. Given the minimal influence of transport during the selected period, the observed diurnal variation of the MAC is governed by the interplay of fresh emissions, aging, and atmospheric removal. These competing effects can be visualized in the two-dimensional relationship between the bulk absorption coefficient and rBC mass (Fig. 7a). Assuming a fresh-BC MAC of $7.13 \text{ m}^2 \text{ g}^{-1}$ (see method, Fig S4b), fresh emission increases both absorption and rBC mass proportionally, producing a linear trajectory (black arrow). Aging enhances absorption without adding rBC mass, resulting in a vertical shift (red arrow). In contrast, removal processes reduce rBC mass and preferentially remove aged particles, yielding a trajectory with a slope larger than $7.13 \text{ m}^2 \text{ g}^{-1}$ (blue arrow).

To isolate absorption changes attributable to the optical variations driven solely by atmospheric aging, linear regressions were applied to the data collected during the respective daytime and nighttime aging periods. This approach estimates the deviation of the measured absorption coefficient from the theoretical baseline, assuming fresh emissions at the same rBC mass concentration. The difference represents the additional absorption coefficient induced by the lensing effect ($b_{E_{\text{abs}}}$), which can



be quantified as follows:

$$b_{E_{\text{abs}}} = b_{\text{abs,obs}} - 7.13 * [\text{rBC}] \quad (4)$$

250 where $[\text{rBC}]$ denotes the rBC core mass concentration. By deriving this $b_{E_{\text{abs}}}$, we eliminate the confounding effects of fresh BC emissions. Although the potential interference from removing cannot be entirely isolated, $b_{E_{\text{abs}}}$ serves as a reliable proxy for characterizing the optical variations driven by daytime and nighttime aging. As $b_{E_{\text{abs}}}$ is dominated by contributions from thickly coated BC particles ($\text{MR} > 3$), we quantified the MAC of thickly coated BC and the temporal rates of MAC change driven by atmospheric aging:

$$255 \quad MAC_{\text{thickly}} = \frac{b_{E_{\text{abs}}} + 7.13 \cdot [\text{rBC}] \cdot f_{\text{coated}}}{[\text{rBC}] \cdot f_{\text{coated}}} \quad (5)$$

$$\frac{MAC_{\text{thickly, max}} - MAC_{\text{thickly, min}}}{\Delta t} \quad (6)$$

where f_{coated} denotes the mass fraction of rBC with high $\text{MR} > 3$, Δt represents the time interval between the minimum and maximum MAC values observed during the respective daytime and nighttime periods. Specifically, aging driven by nocturnal heterogeneous processes led to a MAC increase rate of $0.34 \text{ m}^2 \text{ g}^{-1} \text{ h}^{-1}$. In contrast, daytime photochemical oxidation
 260 substantially accelerated this enhancement, driving the MAC up at a rate of $0.59 \text{ m}^2 \text{ g}^{-1} \text{ h}^{-1}$, approximately 1.7 times the nocturnal rate (Fig. 7b). It should be noted that this rate primarily reflects the optical evolution of thickly coated BC particles. The optical variations associated with the initial morphological transition from fresh fractal aggregates to core-shell structures remain elusive and warrant further investigation. Nevertheless, quantifying these distinct daytime and nighttime absorption enhancement rates provides critical observational constraints.

265 4 Conclusions

This study provides a comprehensive characterization of BC in urban Shenzhen during a sampling period with minimal regional transport influence and dominant local vehicular emissions.

The average rBC mass concentration was $1.2 \mu\text{g m}^{-3}$, with strong correlations to NO_x and CO. The MMD of rBC cores ranged from 155 to 170 nm. By integrating coating information derived from SP2 with chemical composition data from SPAMS
 270 and PMF analysis, we elucidated distinct diurnal aging mechanisms of BC under real-world conditions. Nighttime aging was dominated by heterogeneous uptake of nitrate, driven by liquid-phase reactions and N_2O_5 hydrolysis on BC. In contrast, daytime photochemical aging featured rapid condensation of ammonium nitrate followed by delayed sulfate and oxidized organic formation, with BC enhancing sulfate formation. These sequential processes resulted in bimodal diurnal patterns in coating thickness and secondary species accumulation.

275 The evolving mixing state exerted profound influences on BC optical properties, with the MAC at 532 nm increasing by $\sim 0.8 \text{ m}^2 \text{ g}^{-1}$ overnight and $\sim 1.0 \text{ m}^2 \text{ g}^{-1}$ during the daytime. By tracing the optical variations of thickly coated BC to isolate



the effects of fresh emissions, we determined that the intrinsic MAC enhancement rate driven by daytime photochemistry was $0.59 \text{ m}^2 \text{ g}^{-1} \text{ h}^{-1}$, approximately 1.7 times higher than the $0.34 \text{ m}^2 \text{ g}^{-1} \text{ h}^{-1}$ observed during nocturnal heterogeneous aging. Although photochemical aging proceeds significantly faster, the comparable magnitudes of the total nocturnal and diurnal
280 MAC increments indicate that the rapid daytime coating accumulation was partially offset by the dilution and removal of aged particles during mixing layer expansion.

Data availability. To request the data given in this study, please contact Yin Zhang at the Southern University of Science and Technology, via email (12331308@mail.sustech.edu.cn).

Author contributions. YZ, JZ and XY designed the study. YZ and JZ analyzed the data. YZ wrote the manuscript. All co-authors contributed
285 to discussions and suggestions in finalizing the manuscript.

Competing interests. The authors declare that they have no conflict of interest.

Acknowledgements. This work was supported by the National Natural Science Foundation of China (grant no. 42530609), the Guangdong Provincial Field Observation and Research Station for Coastal Atmosphere and Climate of the Greater Bay Area, Southern University of Science and Technology, Shenzhen, Guangdong, China (grant no. 518055), the Guangdong Provincial Field Observation and Research
290 Station for Coastal Atmosphere and Climate of the Greater Bay Area (grant no. 2021B1212050024), the Shenzhen Science and Technology Program (grant nos. KQTD20210811090048025, KCXFZ20230731093601003), the Ministry of Science and Technology of the People's Republic of China (grant no. 2023YFE0112901), and the High level of special funds (grant no. G03050K001).



References

- 295 Baumgartner, J., Zhang, Y., Schauer, J. J., Huang, W., Wang, Y., and Ezzati, M.: Highway proximity and black carbon from cookstoves as a risk factor for higher blood pressure in rural China, *Proc. Natl. Acad. Sci. U.S.A.*, 111, 13 229–13 234, <https://doi.org/10.1073/pnas.1317176111>, 2014.
- Bond, T. C. and Bergstrom, R. W.: Light Absorption by Carbonaceous Particles: An Investigative Review, *Aerosol Sci. Technol.*, 40, 27–67, <https://doi.org/10.1080/02786820500421521>, 2006.
- 300 Bond, T. C., Doherty, S. J., Fahey, D. W., Forster, P. M., Berntsen, T., DeAngelo, B. J., Flanner, M. G., Ghan, S., Kärcher, B., Koch, D., Kinne, S., Kondo, Y., Quinn, P. K., Sarofim, M. C., Schultz, M. G., Schulz, M., Venkataraman, C., Zhang, H., Zhang, S., Bellouin, N., Guttikunda, S. K., Hopke, P. K., Jacobson, M. Z., Kaiser, J. W., Klimont, Z., Lohmann, U., Schwarz, J. P., Shindell, D., Storelvmo, T., Warren, S. G., and Zender, C. S.: Bounding the role of black carbon in the climate system: A scientific assessment, *J. Geophys. Res. Atmos.*, 118, 5380–5552, <https://doi.org/10.1002/jgrd.50171>, 2013.
- 305 Cappa, C. D., Onasch, T. B., Massoli, P., Worsnop, D. R., Bates, T. S., Cross, E. S., Davidovits, P., Hakala, J., Hayden, K. L., Jobson, B. T., Kolesar, K. R., Lack, D. A., Lerner, B. M., Li, S.-M., Mellon, D., Nuaaman, I., Olfert, J. S., Petäjä, T., Quinn, P. K., Song, C., Subramanian, R., Williams, E. J., and Zaveri, R. A.: Radiative Absorption Enhancements Due to the Mixing State of Atmospheric Black Carbon, *Science*, 337, 1078–1081, <https://doi.org/10.1126/science.1223447>, 2012.
- 310 Cappa, C. D., Zhang, X., Russell, L. M., Collier, S., Lee, A. K. Y., Chen, C., Betha, R., Chen, S., Liu, J., Price, D. J., Sanchez, K. J., McMeeking, G. R., Williams, L. R., Onasch, T. B., Worsnop, D. R., Abbatt, J., and Zhang, Q.: Light Absorption by Ambient Black and Brown Carbon and its Dependence on Black Carbon Coating State for Two California, USA, Cities in Winter and Summer, *J. Geophys. Res. Atmos.*, 124, 1550–1577, <https://doi.org/10.1029/2018JD029501>, 2019.
- Choi, W. and Leu, M.-T.: Nitric Acid Uptake and Decomposition on Black Carbon (Soot) Surfaces: Its Implications for the Upper Troposphere and Lower Stratosphere, *J. Phys. Chem. A*, 102, 7618–7630, <https://doi.org/10.1021/jp981647x>, 1998.
- 315 Fierce, L., Bond, T. C., Bauer, S. E., Mena, F., and Riemer, N.: Black carbon absorption at the global scale is affected by particle-scale diversity in composition, *Nat Commun.*, 7, 12 361, <https://doi.org/10.1038/ncomms12361>, 2016.
- Fuller, K. A., Malm, W. C., and Kreidenweis, S. M.: Effects of mixing on extinction by carbonaceous particles, *J. Geophys. Res. Atmos.*, 104, 15 941–15 954, <https://doi.org/10.1029/1998JD100069>, 1999.
- 320 Gao, R. S., Schwarz, J. P., Kelly, K. K., Fahey, D. W., Watts, L. A., Thompson, T. L., Spackman, J. R., Slowik, J. G., Cross, E. S., Han, J.-H., Davidovits, P., Onasch, T. B., and Worsnop, D. R.: A Novel Method for Estimating Light-Scattering Properties of Soot Aerosols Using a Modified Single-Particle Soot Photometer, *Aerosol Sci. Technol.*, 41, 125–135, <https://doi.org/10.1080/02786820601118398>, 2007.
- Gong, X., Zhang, C., Chen, H., Nizkorodov, S. A., Chen, J., and Yang, X.: Size distribution and mixing state of black carbon particles during a heavy air pollution episode in Shanghai, *Atmos. Chem. Phys.*, 16, 5399–5411, <https://doi.org/10.5194/acp-16-5399-2016>, 2016.
- Guo, Z., Qiu, P., Song, H., Ye, C., Du, Y., and Lu, K.: Insights into black carbon-activated manganese catalysis in atmospheric sulfate production, *Sci. Bull.*, 70, 3659–3666, <https://doi.org/10.1016/j.scib.2025.09.041>, 2025.
- 325 Jacobson, M. Z.: Strong radiative heating due to the mixing state of black carbon in atmospheric aerosols, *Nature*, 409, 695–697, <https://doi.org/10.1038/35055518>, 2001.
- Laborde, M., Schnaiter, M., Linke, C., Saathoff, H., Naumann, K.-H., Möhler, O., Berlenz, S., Wagner, U., Taylor, J. W., Liu, D., Flynn, M., Allan, J. D., Coe, H., Heimerl, K., Dahlkötter, F., Weinzierl, B., Wollny, A. G., Zanatta, M., Cozic, J., Laj, P., Hitznerberger, R.,



- Schwarz, J. P., and Gysel, M.: Single Particle Soot Photometer intercomparison at the AIDA chamber, *Atmos. Meas. Tech.*, 5, 3077–3097, <https://doi.org/10.5194/amt-5-3077-2012>, 2012.
- 330 Laborde, M., Crippa, M., Tritscher, T., Jurányi, Z., Decarlo, P. F., Temime-Roussel, B., Marchand, N., Eckhardt, S., Stohl, A., Baltensperger, U., Prévôt, A. S. H., Weingartner, E., and Gysel, M.: Black carbon physical properties and mixing state in the European megacity Paris, *Atmos. Chem. Phys.*, 13, 5831–5856, <https://doi.org/10.5194/acp-13-5831-2013>, 2013.
- Lan, Z.-J., Huang, X.-F., Yu, K.-Y., Sun, T.-L., Zeng, L.-W., and Hu, M.: Light absorption of black carbon aerosol and its enhancement by mixing state in an urban atmosphere in South China, *Atmos. Environ.*, 69, 118–123, <https://doi.org/https://doi.org/10.1016/j.atmosenv.2012.12.009>, 2013.
- 335 Li, F., Luo, B., Zhai, M., Liu, L., Zhao, G., Xu, H., Deng, T., Deng, X., Tan, H., Kuang, Y., and Zhao, J.: Black carbon content of traffic emissions significantly impacts black carbon mass size distributions and mixing states, *Atmos. Chem. Phys.*, 23, 6545–6558, <https://doi.org/10.5194/acp-23-6545-2023>, 2023.
- 340 Li, L., Huang, Z., Dong, J., Li, M., Gao, W., Nian, H., Fu, Z., Zhang, G., Bi, X., Cheng, P., and Zhou, Z.: Real time bipolar time-of-flight mass spectrometer for analyzing single aerosol particles, *Int. J. Mass Spectrom.*, 303, 118–124, <https://doi.org/10.1016/j.ijms.2011.01.017>, 2011.
- Li, M., Bao, F., Zhang, Y., Sheng, H., Chen, C., and Zhao, J.: Photochemical Aging of Soot in the Aqueous Phase: Release of Dissolved Black Carbon and the Formation of $^1\text{O}_2$, *Environ. Sci. Technol.*, 53, 12 311–12 319, <https://doi.org/10.1021/acs.est.9b02773>, 2019.
- 345 Liu, D., Flynn, M., Gysel, M., Targino, A., Crawford, I., Bower, K., Choularton, T., Jurányi, Z., Steinbacher, M., Hüglin, C., Curtius, J., Kampus, M., Petzold, A., Weingartner, E., Baltensperger, U., and Coe, H.: Single particle characterization of black carbon aerosols at a tropospheric alpine site in Switzerland, *Atmos. Chem. Phys.*, 10, 7389–7407, <https://doi.org/10.5194/acp-10-7389-2010>, 2010.
- Liu, D., Allan, J. D., Young, D. E., Coe, H., Beddows, D., Fleming, Z. L., Flynn, M. J., Gallagher, M. W., Harrison, R. M., Lee, J., Prevot, A. S. H., Taylor, J. W., Yin, J., Williams, P. I., and Zotter, P.: Size distribution, mixing state and source apportionment of black carbon aerosol in London during wintertime, *Atmos. Chem. Phys.*, 14, 10 061–10 084, <https://doi.org/10.5194/acp-14-10061-2014>, 2014.
- 350 Liu, D., Whitehead, J., Alfara, M. R., Reyes-Villegas, E., Spracklen, D. V., Reddington, C. L., Kong, S., Williams, P. I., Ting, Y.-C., Haslett, S., Taylor, J. W., Flynn, M. J., Morgan, W. T., McFiggans, G., Coe, H., and Allan, J. D.: Black-carbon absorption enhancement in the atmosphere determined by particle mixing state, *Nat. Geosci.*, 10, 184–188, <https://doi.org/10.1038/ngeo2901>, 2017.
- Liu, D., Joshi, R., Wang, J., Yu, C., Allan, J. D., Coe, H., Flynn, M. J., Xie, C., Lee, J., Squires, F., Kotthaus, S., Grimmond, S., Ge, X., Sun, Y., and Fu, P.: Contrasting physical properties of black carbon in urban Beijing between winter and summer, *Atmos. Chem. Phys.*, 19, 6749–6769, <https://doi.org/10.5194/acp-19-6749-2019>, 2019.
- 355 Liu, H., Pan, X., Wang, D., Liu, X., Tian, Y., Yao, W., Lei, S., Zhang, Y., Li, J., Lei, L., Xie, C., Fu, P., Sun, Y., and Wang, Z.: Mixing characteristics of black carbon aerosols in a coastal city using the CPMA-SP2 system, *Atmos. Res.*, 265, 105 867, <https://doi.org/10.1016/j.atmosres.2021.105867>, 2022.
- 360 Moteki, N., Kondo, Y., and Ichi Nakamura, S.: Method to measure refractive indices of small nonspherical particles: Application to black carbon particles, *J. Aerosol Sci.*, 41, 513–521, <https://doi.org/10.1016/j.jaerosci.2010.02.013>, 2010.
- Peng, J., Hu, M., Guo, S., Du, Z., Zheng, J., Shang, D., Levy Zamora, M., Zeng, L., Shao, M., Wu, Y.-S., Zheng, J., Wang, Y., Glen, C. R., Collins, D. R., Molina, M. J., and Zhang, R.: Markedly enhanced absorption and direct radiative forcing of black carbon under polluted urban environments, *Proc. Natl. Acad. Sci. U.S.A.*, 113, 4266–4271, <https://doi.org/10.1073/pnas.1602310113>, 2016.



- 365 Petzold, A., Ogren, J. A., Fiebig, M., Laj, P., Li, S.-M., Baltensperger, U., Holzer-Popp, T., Kinne, S., Pappalardo, G., Sugimoto, N., Wehrli, C., Wiedensohler, A., and Zhang, X.-Y.: Recommendations for reporting "black carbon" measurements, *Atmos. Chem. Phys.*, 13, 8365–8379, <https://doi.org/10.5194/acp-13-8365-2013>, 2013.
- Popovicheva, O. B., Chichayeva, M. A., Evangelidou, N., Eckhardt, S., Diapouli, E., and Kasimov, N. S.: Multi-year black carbon observations and modeling close to the largest gas flaring and wildfire regions in the Western Siberian Arctic, *Atmos. Chem. Phys.*, 25, 7719–7739, <https://doi.org/10.5194/acp-25-7719-2025>, 2025.
- 370 Prince, A., Wade, J., Grassian, V., Kleiber, P., and Young, M.: Heterogeneous reactions of soot aerosols with nitrogen dioxide and nitric acid: atmospheric chamber and Knudsen cell studies, *Atmos. Environ.*, 36, 5729–5740, [https://doi.org/10.1016/S1352-2310\(02\)00626-X](https://doi.org/10.1016/S1352-2310(02)00626-X), 2002.
- Riemer, N., West, M., Zaveri, R., and Easter, R.: Estimating black carbon aging time-scales with a particle-resolved aerosol model, *J. Aerosol Sci.*, 41, 143–158, <https://doi.org/10.1016/j.jaerosci.2009.08.009>, 2010.
- 375 Schwarz, J. P., Gao, R. S., Fahey, D. W., Thomson, D. S., Watts, L. A., Wilson, J. C., Reeves, J. M., Darbeheshti, M., Baumgardner, D. G., Kok, G. L., Chung, S. H., Schulz, M., Hendricks, J., Lauer, A., Kärcher, B., Slowik, J. G., Rosenlof, K. H., Thompson, T. L., Langford, A. O., Loewenstein, M., and Aikin, K. C.: Single-particle measurements of midlatitude black carbon and light-scattering aerosols from the boundary layer to the lower stratosphere, *J. Geophys. Res. Atmos.*, 111, <https://doi.org/10.1029/2006JD007076>, 2006.
- Sedlacek III, A. J., Lewis, E. R., Kleinman, L., Xu, J., and Zhang, Q.: Determination of and evidence for non-core-shell structure of particles containing black carbon using the Single-Particle Soot Photometer (SP2), *Geophys. Res. Lett.*, 39, <https://doi.org/10.1029/2012GL050905>, 2012.
- 380 Song, X.-H., Hopke, P. K., Fergenson, D. P., and Prather, K. A.: Classification of Single Particles Analyzed by ATOFMS Using an Artificial Neural Network, *ART-2A, Anal. Chem.*, 71, 860–865, <https://doi.org/10.1021/ac9809682>, 1999.
- Spencer, M. T. and Prather, K. A.: Using ATOFMS to Determine OC/EC Mass Fractions in Particles, *Aerosol Sci. Technol.*, 40, 585–594, <https://doi.org/10.1080/02786820600729138>, 2006.
- 385 Stephens, M., Turner, N., and Sandberg, J.: Particle identification by laser-induced incandescence in a solid-state laser cavity, *Appl. Opt.*, 42, 3726–3736, <https://doi.org/10.1364/AO.42.003726>, 2003.
- Sun, J. Y., Wu, C., Wu, D., Cheng, C., Li, M., Li, L., Deng, T., Yu, J. Z., Li, Y. J., Zhou, Q., Liang, Y., Sun, T., Song, L., Cheng, P., Yang, W., Pei, C., Chen, Y., Cen, Y., Nian, H., and Zhou, Z.: Amplification of black carbon light absorption induced by atmospheric aging: temporal variation at seasonal and diel scales in urban Guangzhou, *Atmos. Chem. Phys.*, 20, 2445–2470, <https://doi.org/10.5194/acp-20-2445-2020>, 2020.
- 390 Wang, X., Zhang, Y., Chen, H., Yang, X., Chen, J., and Geng, F.: Particulate Nitrate Formation in a Highly Polluted Urban Area: A Case Study by Single-Particle Mass Spectrometry in Shanghai, *Environ. Sci. Technol.*, 43, 3061–3066, <https://doi.org/10.1021/es8020155>, 2009.
- Wang, Y., Li, W., Huang, J., Liu, L., Pang, Y., He, C., Liu, F., Liu, D., Bi, L., Zhang, X., and Shi, Z.: Nonlinear Enhancement of Radiative Absorption by Black Carbon in Response to Particle Mixing Structure, *Geophys. Res. Lett.*, 48, e2021GL096437, <https://doi.org/10.1029/2021GL096437>, 2021.
- 395 Wei, J., Niu, Y.-B., Tang, M.-X., Peng, Y., Cao, L.-M., He, L.-Y., and Huang, X.-F.: Characterizing formation mechanisms of secondary aerosols on black carbon in a megacity in South China, *Sci. Total Environ.*, 859, 160 290, <https://doi.org/10.1016/j.scitotenv.2022.160290>, 2023.
- 400 Wu, Y., Cheng, T., Liu, D., Allan, J. D., Zheng, L., and Chen, H.: Light Absorption Enhancement of Black Carbon Aerosol Constrained by Particle Morphology, *Environ. Sci. Technol.*, 52, 6912–6919, <https://doi.org/10.1021/acs.est.8b00636>, 2018.



- Xue, L., Gu, R., Wang, T., Wang, X., Saunders, S., Blake, D., Louie, P. K. K., Luk, C. W. Y., Simpson, I., Xu, Z., Wang, Z., Gao, Y., Lee, S., Mellouki, A., and Wang, W.: Oxidative capacity and radical chemistry in the polluted atmosphere of Hong Kong and Pearl River Delta region: analysis of a severe photochemical smog episode, *Atmos. Chem. Phys.*, 16, 9891–9903, <https://doi.org/10.5194/acp-16-9891-2016>, 2016.
- 405
- Yang, Z., Ma, N., Wang, Q., Li, G., Pan, X., Dong, W., Zhu, S., Zhang, S., Gao, W., He, Y., Xie, L., Zhang, Y., Kuhn, U., Xu, W., Kuang, Y., Tao, J., Hong, J., Zhou, G., Sun, Y., Su, H., and Cheng, Y.: Characteristics and source apportionment of black carbon aerosol in the North China Plain, *Atmos. Res.*, 276, 106 246, <https://doi.org/10.1016/j.atmosres.2022.106246>, 2022.
- Yuan, C., Zheng, J., Ma, Y., Jiang, Y., Li, Y., and Wang, Z.: Significant restructuring and light absorption enhancement of black carbon particles by ammonium nitrate coating, *Environ. Pollut.*, 262, 114 172, <https://doi.org/10.1016/j.envpol.2020.114172>, 2020.
- 410
- Zauscher, M. D., Wang, Y., Moore, M. J. K., Gaston, C. J., and Prather, K. A.: Air Quality Impact and Physicochemical Aging of Biomass Burning Aerosols during the 2007 San Diego Wildfires, *Environ. Sci. Technol.*, 47, 7633–7643, <https://doi.org/10.1021/es4004137>, 2013.
- Zhai, J., Yang, X., Li, L., Bai, B., Liu, P., Huang, Y., Fu, T.-M., Zhu, L., Zeng, Z., Tao, S., Lu, X., Ye, X., Wang, X., Wang, L., and Chen, J.: Absorption Enhancement of Black Carbon Aerosols Constrained by Mixing-State Heterogeneity, *Environ. Sci. Technol.*, 56, 1586–1593, <https://doi.org/10.1021/acs.est.1c06180>, 2022a.
- 415
- Zhai, J., Yang, X., Li, L., Ye, X., Chen, J., Fu, T., Zhu, L., Shen, H., Ye, J., Wang, C., and Tao, S.: Direct Observation of the Transitional Stage of Mixing-State-Related Absorption Enhancement for Atmospheric Black Carbon, *Geophys. Res. Lett.*, 49, e2022GL101 368, <https://doi.org/10.1029/2022GL101368>, 2022b.
- Zhai, J., Shao, S., Yang, X., Zeng, Y., Fu, T.-M., Zhu, L., Shen, H., Ye, J., Wang, C., and Tao, S.: Chemically Resolved Respiratory Deposition of Ultrafine Particles Characterized by Number Concentration in the Urban Atmosphere, *Environ. Sci. Technol.*, 58, 16 507–16 516, <https://doi.org/10.1021/acs.est.4c03279>, 2023.
- 420
- Zhai, J., Zhang, Y., Liu, P., Zhang, Y., Zhang, A., Zeng, Y., Cai, B., Zhang, J., Xing, C., Yang, H., Wang, X., Ye, J., Wang, C., Fu, T.-M., Zhu, L., Shen, H., Tao, S., and Yang, X.: Source-dependent optical properties and molecular characteristics of atmospheric brown carbon, *Atmos. Chem. Phys.*, 25, 7959–7972, <https://doi.org/10.5194/acp-25-7959-2025>, 2025.
- 425
- Zhang, G., Fu, Y., Peng, X., Sun, W., Shi, Z., Song, W., Hu, W., Chen, D., Lian, X., Li, L., Tang, M., Wang, X., and Bi, X.: Black Carbon Involved Photochemistry Enhances the Formation of Sulfate in the Ambient Atmosphere: Evidence From In Situ Individual Particle Investigation, *J. Geophys. Res. Atmos.*, 126, e2021JD035 226, <https://doi.org/10.1029/2021JD035226>, 2021.
- Zhang, R., Khalizov, A. F., Pagels, J., Zhang, D., Xue, H., and McMurry, P. H.: Variability in morphology, hygroscopicity, and optical properties of soot aerosols during atmospheric processing, *Proc. Natl. Acad. Sci. U.S.A.*, 105, 10 291–10 296, <https://doi.org/10.1073/pnas.0804860105>, 2008.
- 430
- Zhang, Y., Zhang, Q., Cheng, Y., Su, H., Li, H., Li, M., Zhang, X., Ding, A., and He, K.: Amplification of light absorption of black carbon associated with air pollution, *Atmos. Chem. Phys.*, 18, 9879–9896, <https://doi.org/10.5194/acp-18-9879-2018>, 2018.
- Zhang, Y., Wang, J., Wu, N., Ouyang, X., Li, G., Cheng, Y., Zhang, Q., Ding, A., and Su, H.: The Contribution of Black Carbon Containing Particles to PM_{2.5}: Variability, Drivers, and Impacts, *Environ. Sci. Technol.*, 59, 5155–5163, <https://doi.org/10.1021/acs.est.5c00675>, 2025.
- 435
- Zhou, Q., Cheng, C., Yang, S., Yuan, M., Meng, J., Gong, H., Zhong, Q., Zhang, Y., Xie, Y., Zhou, Z., and Li, M.: Enhanced mixing state of black carbon with nitrate in single particles during haze periods in Zhengzhou, China, *J. Environ. Sci.*, 111, 185–196, <https://doi.org/10.1016/j.jes.2021.03.031>, 2022.

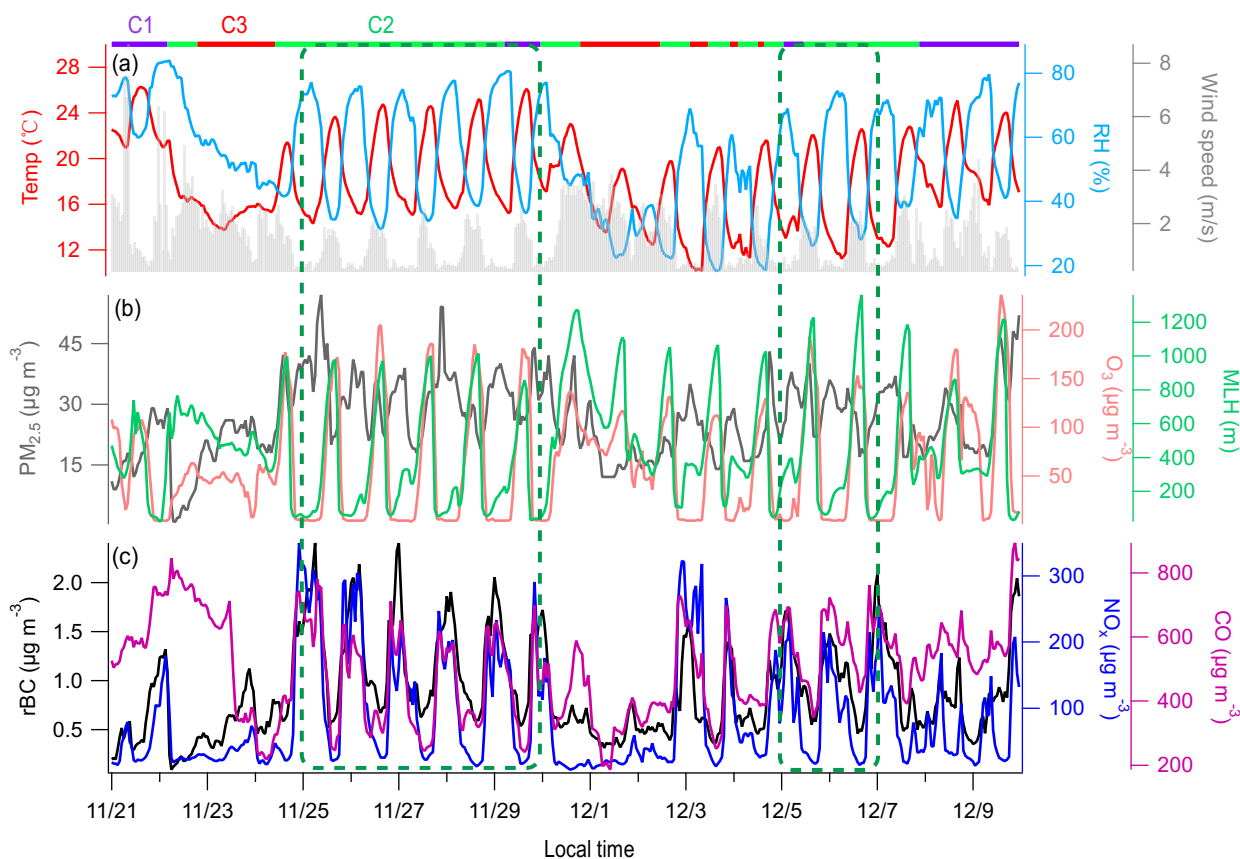


Figure 1. Temporal variations of meteorological parameters and pollutant mass concentrations with 60-min resolution. (a) Temperature, relative humidity (RH), and wind speed, (b) $PM_{2.5}$, O_3 , and mixing layer height, (c) rBC and NO_x . The time period enclosed by the green box is defined as predominantly influenced by local emissions and the discussion focuses on these data.

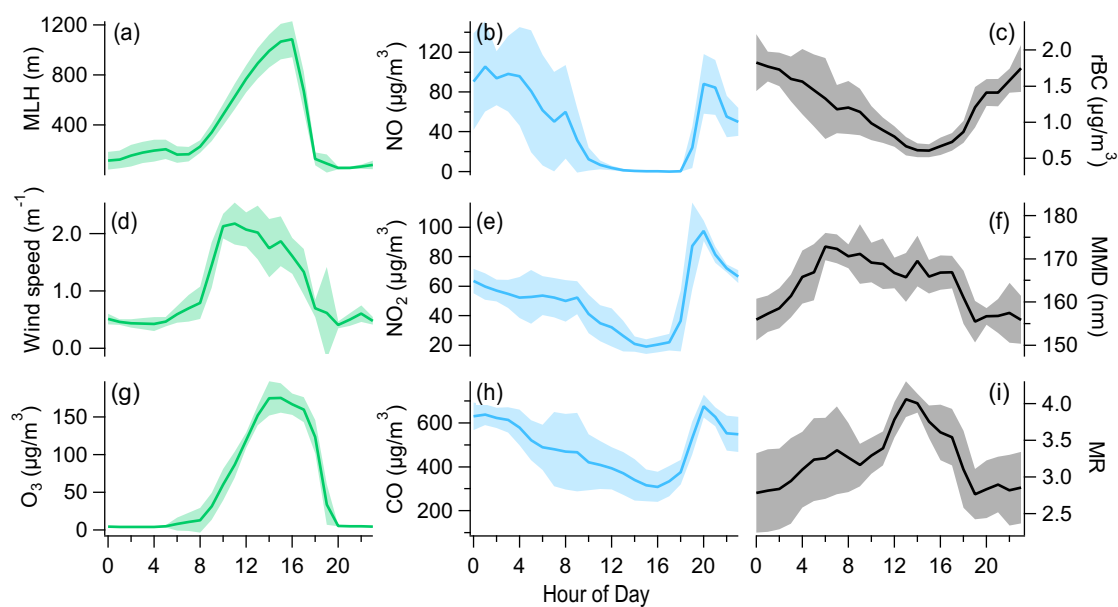


Figure 2. The diurnal variations of (a) MLH, (b) NO mass concentration, (c) rBC mass concentration, (d) wind speed, (e) NO₂ mass concentration, (f) MMD, (g) O_x mass concentration, (h) CO mass concentration, and (i) MR. Data points denote hourly mean values, and the shaded areas represent ± 1 standard deviation.

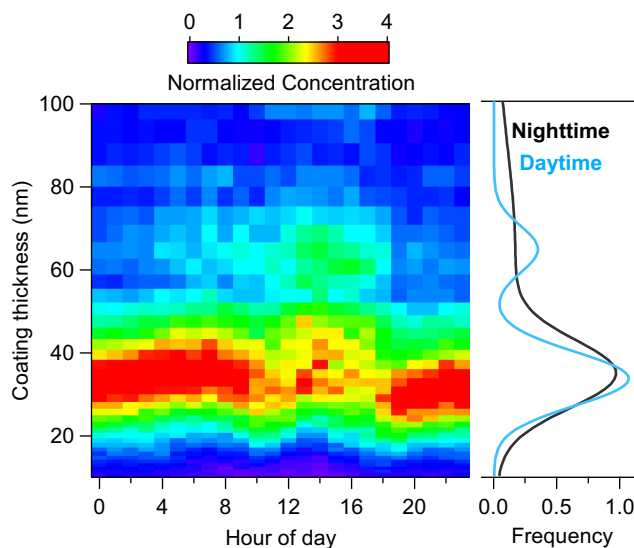


Figure 3. Diurnal variation in the coating thickness of rBC particles. The left panel presents a heatmap showing the distribution of coating thickness. The right panel shows normalized frequency distributions of coating thickness for nighttime (00:00–06:00) and daytime (09:00–14:00) periods, with overlaid lognormal fits to highlight differences. It should be noted that the diurnal variation of the coating thickness presented here is only for the rBC core with a diameter of 160 ± 20 nm, which was the dominant contributor to the total rBC mass concentration.

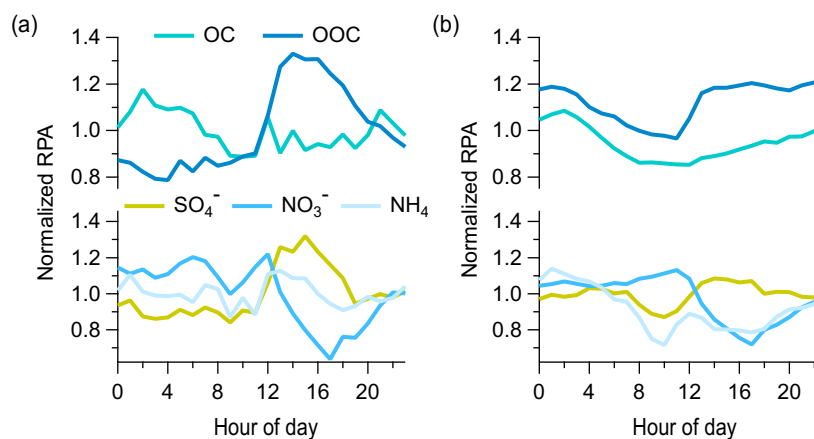


Figure 4. The normalized relative peak areas (RPA) of BC-containing particles (a) and non-BC particles (b) measured by SPAMS. OC is the sum of the representative organic species (m/z 27 [$C_2H_3^+$], 29 [$C_2H_5^+$], 51 [$C_4H_3^+$], -26 [CN^-]), OOC represents the sum of the oxygenated organic species (m/z 43 [CH_3CO^+], -57 [$C_2HO_2^-$], -89 [$C_2O_4H^-$]), SO_4^- represents m/z -97 [SO_4^-], NO_3^- represents m/z -62 [NO_3^-], and NH_4^+ represents m/z 18 [NH_4^+]. The RPA at each time point was normalized by dividing it by the average RPA over the entire sampling period.

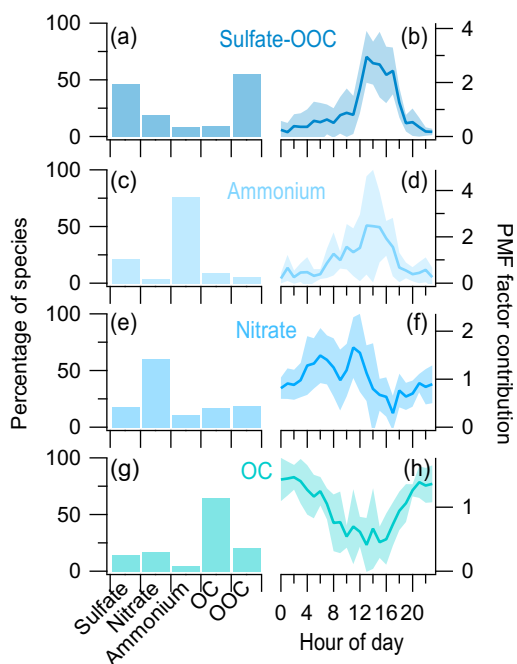


Figure 5. (a, c, e, g) PMF-resolved four source profiles and (b, d, f, h) their diurnal profile of contributions.

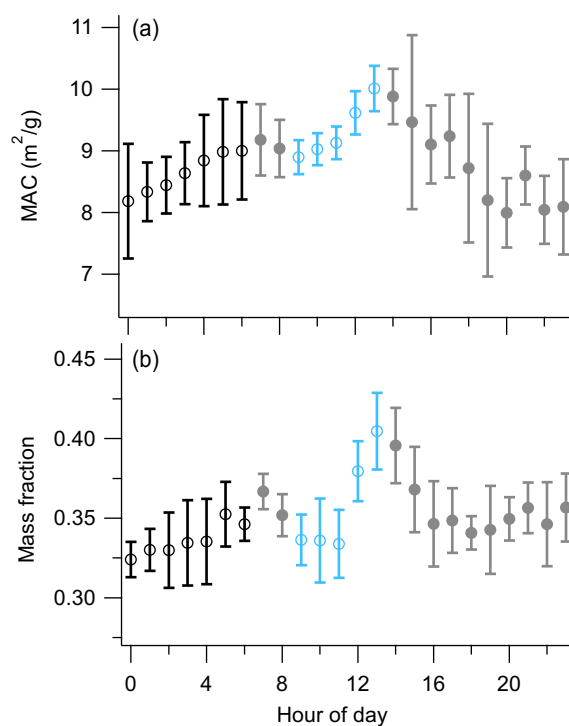


Figure 6. (a) Diurnal variation in the MAC of rBC at 532 nm. (b) The mass fraction of rBC exhibiting absorption enhancement

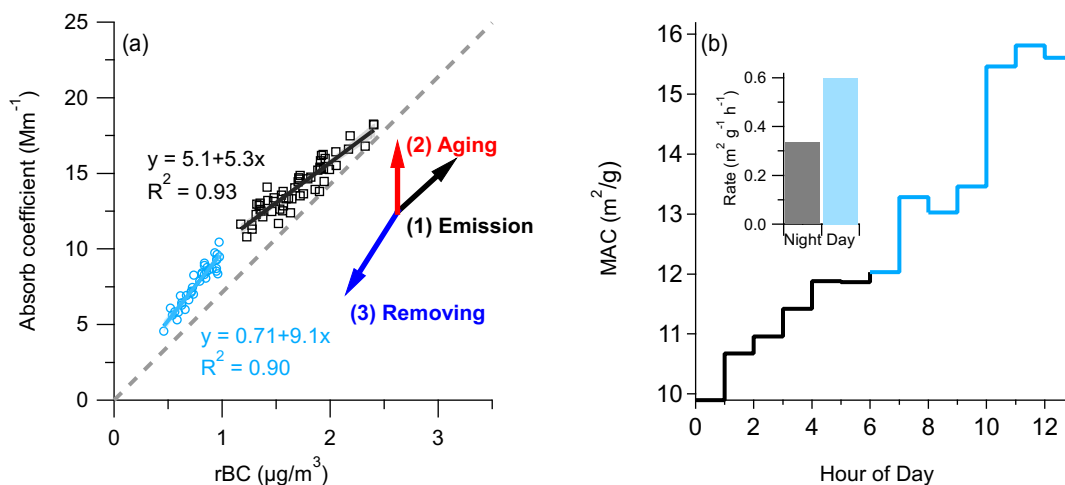


Figure 7. (a) Scatter plot of the light absorption coefficient and rBC mass concentration, with data points colored by daytime (blue) and nighttime (black) periods. The gray dashed line indicates the expected relationship assuming all rBC particles are freshly emitted. Red arrows denote the directional shifts in the scatter plot induced by (1) fresh emissions, (2) atmospheric aging, and (3) removal processes; (b) The MAC enhancement rates during daytime and nighttime.